# Supplementary Data

**Table S1** Literature summary of the mechanical integrity and compression stress-strain data of bulk nanoporous metals obtained by dealloying.

| Precursor alloy nominal composition (at.%) | Precursor alloy phase | Nanoporous metal | As-dealloyed structure | Ligament diameter (nm) | Porosity (%) | Compressive strength (MPa) | Compressive strain (%) | Comments | Extracted figures | Ref |
|---|---|---|---|---|---|---|---|---|---|---|
| Mn-40Cu | Solid solution | Cu | Hierarchical | 44.7 | 58.08 | 163 | 3.09 | Mn-20Cu exhibit brittle fracture upon dealloying. Mn-50Cu exhibited surface passivation upon dealloying. Mn-30, 40Cu exhibited a robust lattice-like structure. Robust nature of the unique structure was attributed to the precursor alloy microsegregation which produced an advantageous lattice-like macrostructure. Inhibited passivation of the segregated microstructure ensured complete dealloying of the interdendritic matrix containing a very low Mn content, resulting in reduced volumetric stresses. Compression testing performed on dealloyed Mn-40Cu specimens (dealloyed specimen pictured). | 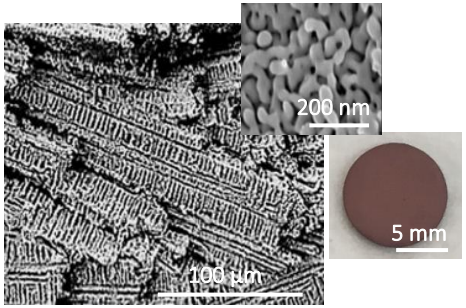 | **This work** |
| $Cu_{20}Ni_{10}Mn_{70}$ | Solid solution | Cu | Monolithic | 13-40 | 69 | ~52.5-18 | 3-11 | Low cracking. High strength of np Cu attributed to the small ligament size compared to microporous Cu structures. (Up to 7 MPa for Cu foams). Due to the high surface area to volume ratio of np Cu, the nature of the surface may influence its mechanical performance. As described earlier, Cu and Ni readily form an oxide layer on the materials surface. During deformation, the dislocation motion can be impeded through pinning of dislocation endpoints at the adsorbed surface layer, a mechanism known as "adsorption locking" | 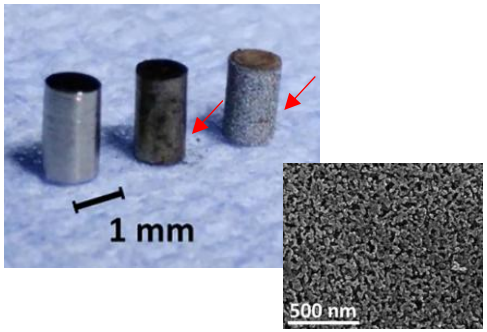 | [1] |

| Precursor alloy nominal composition (at.%) | Precursor alloy phase | Nanoporous metal | As-dealloyed structure | Ligament diameter (nm) | Porosity (%) | Compressive strength (MPa) | Compressive strain (%) | Comments | Extracted figures | Ref |
|---|---|---|---|---|---|---|---|---|---|---|
| Cu-25Au | Solid solution | Au | Monolithic | 10 | - | 70 | 2 | Cracking in specimens with higher electrochemical dealloying potentials resulting in improved mechanical integrity and lesser cracking. | 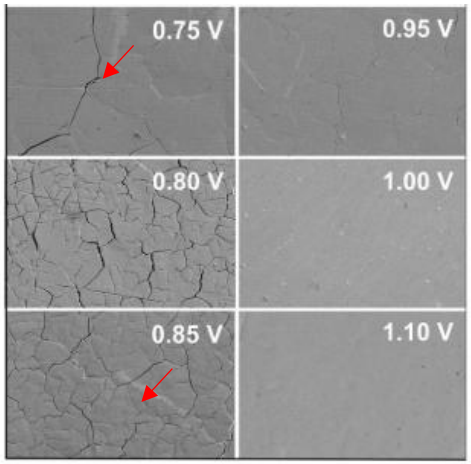  | [2] |
| Al-22Cu | Intermetallic | Cu | Hierarchical | 27 | 80 | 4.5-5.8 | 3.5-4.5 | Brittle failure under compression. | 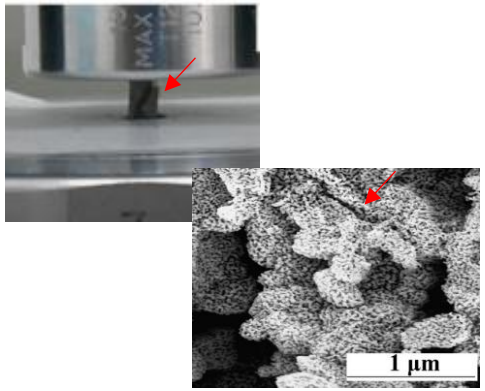  | [3] |

| Precursor alloy nominal composition (at.%) | Precursor alloy phase | Nanoporous metal | As-dealloyed structure | Ligament diameter (nm) | Porosity (%) | Compressive strength (MPa) | Compressive strain (%) | Comments | Extracted figures | Ref |
|---|---|---|---|---|---|---|---|---|---|---|
| Al-30, 33, 40, 50Cu | Intermetallic | Cu | Monolithic/ Hierarchical | | 56.3-73.9 | 2.71-17.18 | ~4-29 | Low stress required to fracture. Strain to failure is quite variable. Interestingly, lower precursor alloy Cu fraction resulted in higher ductility in as-dealloyed specimens. Strain to failure is reported to be approaching 60 % for all specimens, however, evidence of brittle fracture is evident at lower strain.<br><br>As-dealloyed specimen mechanical integrity not mentioned, cracks in SEM micrographs. | 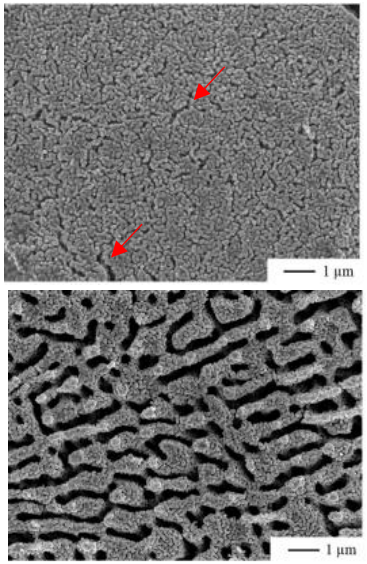 | [4] |
| Al-25Cu | Amorphous/ Intermetallic | Cu | Monolithic/ Hierarchical | 19.7-46.9 | - | - | - | Some specimens displayed severe cracking after dealloying while others did not – depending on the solution used. Mechanism not explored. | 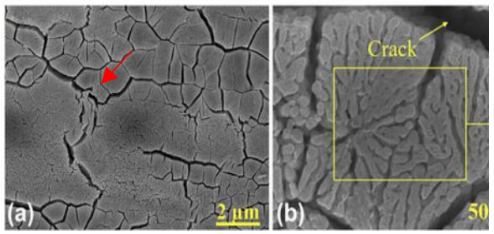 | [5] |

| Precursor alloy nominal composition (at.%) | Precursor alloy phase | Nanoporous metal | As-dealloyed structure | Ligament diameter (nm) | Porosity (%) | Compressive strength (MPa) | Compressive strain (%) | Comments | Extracted figures | Ref |
|---|---|---|---|---|---|---|---|---|---|---|
| Mn-30Cu | Solid solution | Cu | Monolithic | 16-125 | 70 | - | - | Cracking in as-dealloyed samples despite being a solid solution. Cracking noted to be unavoidable. | 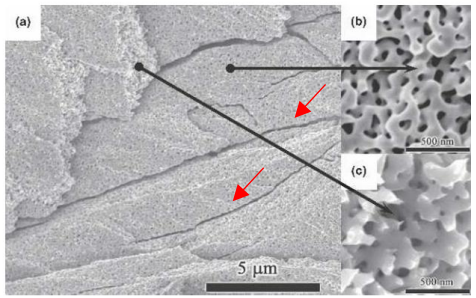  | [6] |
| Mg-33Cu and Mg-36.7 | Intermetallic<br>$CuMg_2$<br>CuMg | Cu | Monolithic/hierarchical | Monolithic – 36<br>Hierarchical - 34 | Monolithic -73<br>Hierarchical - Unknown | Monolithic – 8.5<br>Hierarchical – 15.4 | ~7.5 % (Hierarchical) | Cracks in as-dealloyed samples. Hierarchical structure showed improved hardness and strength over monolithic structure. Attributed to load-bearing and crack-arresting effects of the embedded undealloyed intermetallic particles.<br><br>Drop off in stress and jaggered stress-strain profile at ~ 6 % strain indicates brittle fracture. Continual loading occurs after fracture. | 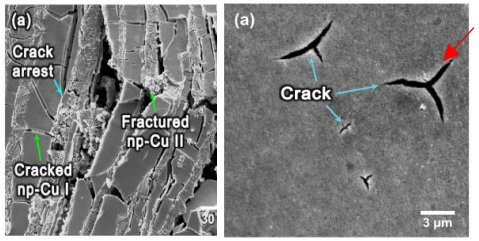  | [7] |
| Ag-7Au | Solid solution | Au | Hierarchical | 45-180 | 62-68 | 9-26 | >40 | As-dealloyed samples are free of microcracks. Lower (nanopores) and upper (struts) hierarchical levels.<br><br>The upper-hierarchy–level struts of N3 PG appear to support ductile plastic bending, whereas NPG is typically brittle when loaded in bending.<br><br>Two stage dealloying process allows for high Au fraction within the macro ligaments before complete dealloying. This was said to improve mechanical integrity before complete dealloying/ | 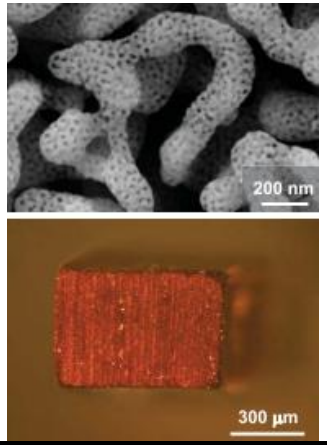  | [8] |

| Precursor alloy nominal composition (at.%) | Precursor alloy phase | Nanoporous metal | As-dealloyed structure | Ligament diameter (nm) | Porosity (%) | Compressive strength (MPa) | Compressive strain (%) | Comments | Extracted figures | Ref |
|---|---|---|---|---|---|---|---|---|---|---|
| Cu30Mg25Ca45, Cu35Mg25Ca40, Cu40Mg25Ca35 and Cu45Mg25Ca30 | Intermetallic | Cu | Hierarchical | 55-195 | - | - | - | Substantial cracking in all specimens. | 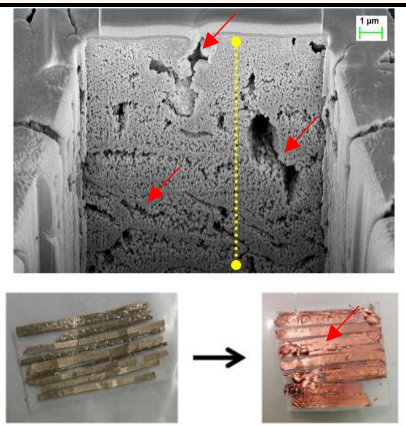  | [9] |
| Ni-20Pd | Solid solution | Pd | Monolithic | 22 | - | - | - | Significant cracking resulting in sample collapsing. | 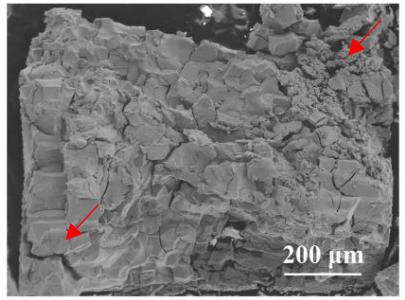  | [10] |

| Precursor alloy nominal composition (at.%) | Precursor alloy phase | Nanoporous metal | As-dealloyed structure | Ligament diameter (nm) | Porosity (%) | Compressive strength (MPa) | Compressive strain (%) | Comments | Extracted figures | Ref |
|---|---|---|---|---|---|---|---|---|---|---|
| Ag-20, 25, 30, 35Au | Solid solution | Au | Monolithic | - | - | - | - | Cracking developing after dealloying all compositions. Most significant cracking occurred in Ag-20Au specimens.<br><br>Rapid surface passivation occurred in Ag-40Au specimens. | 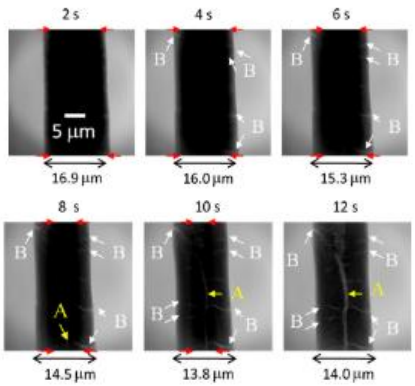 | [11] |
| Al-30, 33, 40, 50Cu | Intermetallic | Cu | Monolithic/Hierarchical | 100-500 | - | - | - | Cracking in Al-33Cu specimens. Higher atomic fractions of Cu showed improved mechanical integrity. | 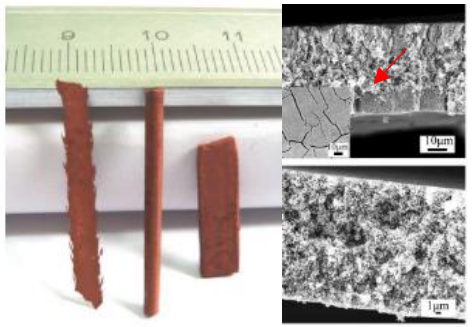 | [12] |
| Mg-33, 40, 50, 60, 67 | Intermetallic | Cu | Monolithic/Hierarchical | 148-272 | - | - | - | Cracking in all specimens. | 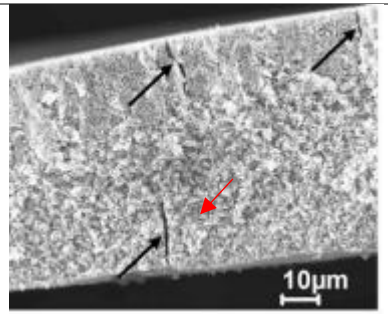 | [13] |

| Precursor alloy nominal composition (at.%) | Precursor alloy phase | Nanoporous metal | As-dealloyed structure | Ligament diameter (nm) | Porosity (%) | Compressive strength (MPa) | Compressive strain (%) | Comments | Extracted figures | Ref |
|---|---|---|---|---|---|---|---|---|---|---|
| $(Al_{75}Cu_{17}Mg_8)_{97}Ni_3$ $Al_{70}Cu_{18}Mg_{12}$ | Amorphous | Cu | Monolithic | 10-30 | - | - | - | Cracking in all specimens. | 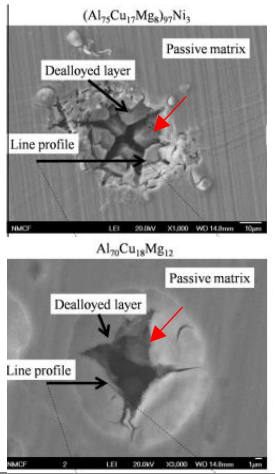  | [14] |
| Mn-42Cu | Solid solution | Cu | Monolithic/hierarchical | 75-480 | 41-73 | 6.5 (Monolithic) ~25-200 (Hierarchical) | ~3 % (monolithic) ~12-20 % (Hierarchical) | Significant cracking of dealloyed monolithic nanoporous Cu specimens. Loosely packed powderized nanoporous samples were sintered to form a hierarchical porous Cu structure. Adept solution to robust mechanical integrity at the cost of heavily coarsened ligaments(up to 480 nm). | 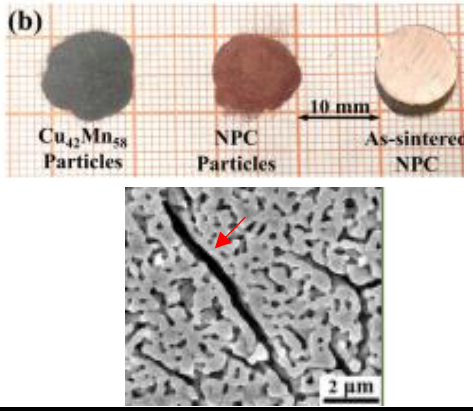  | [15] |

| Precursor alloy nominal composition (at.%) | Precursor alloy phase | Nanoporous metal | As-dealloyed structure | Ligament diameter (nm) | Porosity (%) | Compressive strength (MPa) | Compressive strain (%) | Comments | Extracted figures | Ref |
|---|---|---|---|---|---|---|---|---|---|---|
| $Ti_{50}Cu_{46}Co_4$ | Amorphous | Cu | Monolithic | 10-60 nm | - | - | - | Cracking in all nanoporous Cu specimens produced by increasing dealloying time in a 0.23 M HCl solution. | 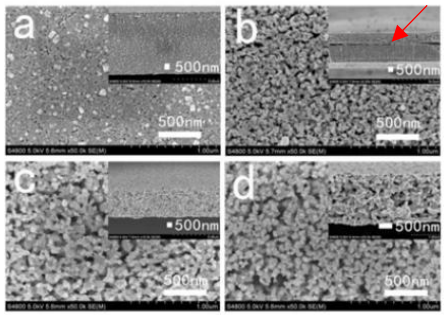  | [16] |
| Cu-25Ag | Intermetallic | Ag | Hierarchical | 70-190 | - | - | - | Cracking observed with and without ultrasonication. Ultrasonication accelerated cracking. | 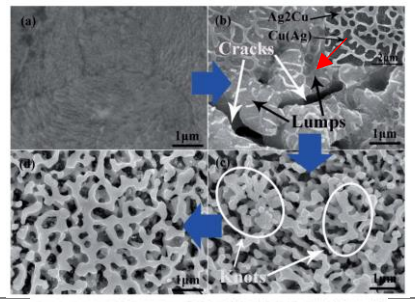  | [17] |
| Zn-20Cu | Solid solution | Cu | Monolithic | 21-128 | - | - | - | Micro-cracks are observed in the dealloyed ribbons due to the strong volume changes during the Zn dissolution and the resulting crystal transformation from hexagonal close packed (hcp) to face-centered cubic (fcc). | 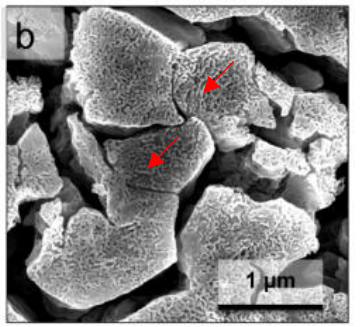  | [18] |

| Precursor alloy nominal composition (at.%) | Precursor alloy phase | Nanoporous metal | As-dealloyed structure | Ligament diameter (nm) | Porosity (%) | Compressive strength (MPa) | Compressive strain (%) | Comments | Extracted figures | Ref |
|---|---|---|---|---|---|---|---|---|---|---|
| Mg-12Cu | Intermetallic | Cu | Hierarchical | 20 | - | - | - | Cracking found to be unavoidable. Massive and rapid extension of cracks. | 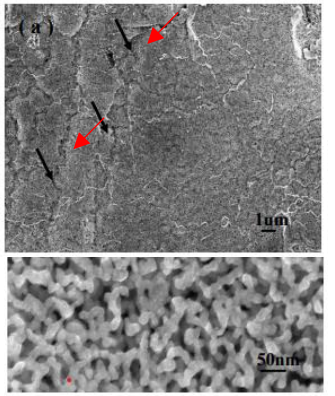  | [19] |
| Cu-10Au | Solid solution | Au | Monolithic | 36-43 | - | - | - | Significant cracking forming primarily at the grain boundaries of the precursor Cu-10Au alloy. | 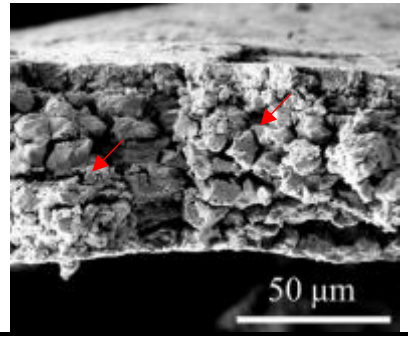  | [20] |

| Precursor alloy nominal composition (at.%) | Precursor alloy phase | Nanoporous metal | As-dealloyed structure | Ligament diameter (nm) | Porosity (%) | Compressive strength (MPa) | Compressive strain (%) | Comments | Extracted figures | Ref |
|---|---|---|---|---|---|---|---|---|---|---|
| Al-25, 38, 50Cu | Intermetallic | Cu | Hierarchical | 40-120 | 57.07-69.52 | ~01.5-8.5 | 15-20 | Cracks present in all dealloyed specimens. Low compressive strength and strain to failure.<br><br>It is noted that nanoporous Cu exhibits more brittle behaviour than nanoporous Au, might be related to the oxidation on the sample surface.<br><br>Mechanical properties improved by impregnating pores with an epoxy to form a composite material. However, functional properties are lost. | 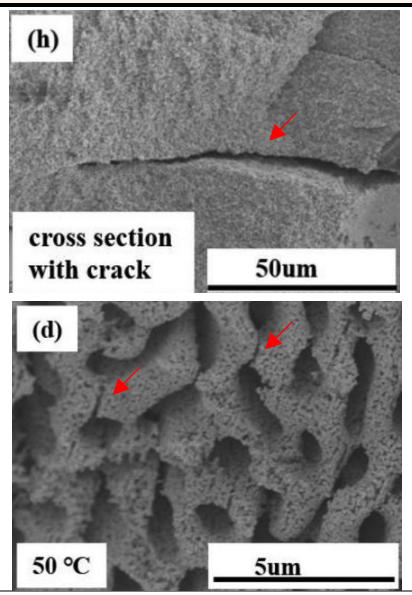 | [21] |
| Al-17, 25, 33 Cu | Intermetallic | Cu | Hierarchical | 25-50 | - | - | - | Cracking observed in all specimens. Mechanical integrity of samples not discussed. | 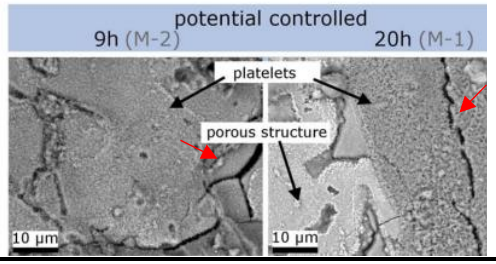 | [22] |

| Precursor alloy nominal composition (at.%) | Precursor alloy phase | Nanoporous metal | As-dealloyed structure | Ligament diameter (nm) | Porosity (%) | Compressive strength (MPa) | Compressive strain (%) | Comments | Extracted figures | Ref |
|---|---|---|---|---|---|---|---|---|---|---|
| Zr-30, 40, 50, 60 Cu | Amorphous | Cu | Monolithic | 20-35 | - | - | - | Top surface cracking present from both the lowest to the highest Cu fractions. | 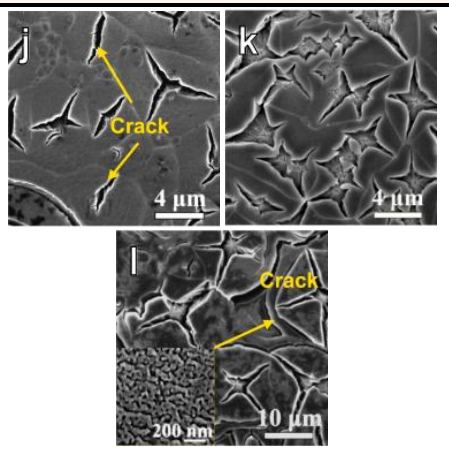 | [23] |
| Al-20, 35Cu Zn-20Cu | Intermetallic | Cu | Hierarchical | 21-28 | 57-78 | - | - | Top surface intergranular cracking present in all specimens. | 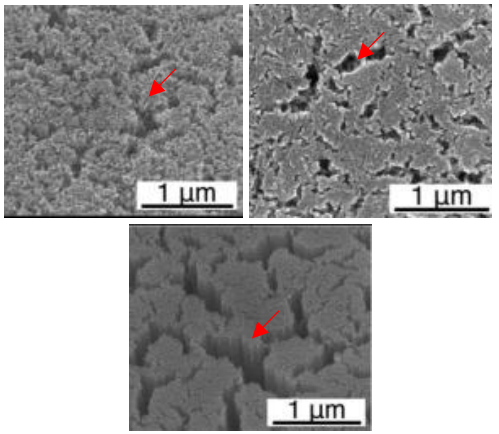 | [24] |

| Precursor alloy nominal composition (at.%) | Precursor alloy phase | Nanoporous metal | As-dealloyed structure | Ligament diameter (nm) | Porosity (%) | Compressive strength (MPa) | Compressive strain (%) | Comments | Extracted figures | Ref |
|---|---|---|---|---|---|---|---|---|---|---|
| Al-18, 20, 24, 32 | Intermetallic | Cu | Hierarchical | 15-60 | 76-88 | ~0.16-10 | ~3.5-8 | Increasing compressive strength and strain to failure with increasing Cu content. Cracking in all as-dealloyed specimens. | 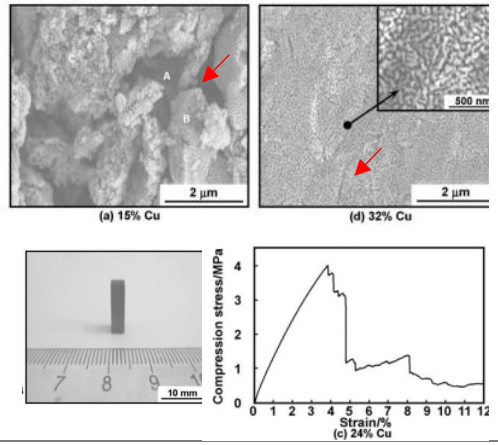 | [25] |
| Al-65Cu | Intermetallic | Cu | Composite | 40 | - | 45 | 8 | Low compressive strength and strain to failure. Mechanical integrity of specimens not discussed. Composite structure intermetallic/nanoporous. | 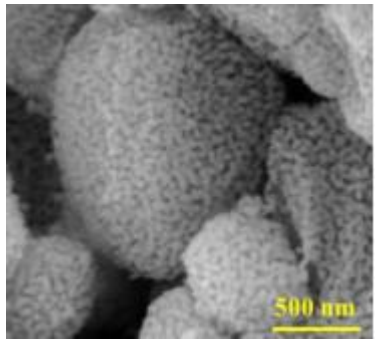 | [26] |

| Precursor alloy nominal composition (at.%) | Precursor alloy phase | Nanoporous metal | As-dealloyed structure | Ligament diameter (nm) | Porosity (%) | Compressive strength (MPa) | Compressive strain (%) | Comments | Extracted figures | Ref |
|---|---|---|---|---|---|---|---|---|---|---|
| **Al-30, 40Cu** | Intermetallic | Cu | Hierarchical | 30-100 | - | - | - | Destructive cracking in all as-dealloyed specimens. | 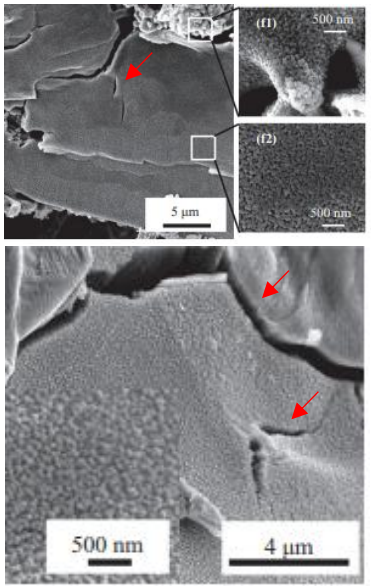 | [27] |

**Table S2** Summary of bulk compression stress-strain data obtained from open cell Cu foams.

| Fabrication method | Strut diameter (μm) | Porosity (%) | Compressive strength (MPa) | Compressive strain (%) | Comments | Extracted figures | Ref |
|---|---|---|---|---|---|---|---|
| Freeze casting | 12 | 62.8-72.9 | 19.4-29.4 | 3 | Brittle fracture at a compressive strain approaching 3 %. A stress drop and jaggered stress-strain profile correlates with visual brittle fracture approaching 3 % strain.<br><br>Continual loading results in compression of broken struts.<br><br>Analogous to examples of dealloying fabrication of nanoporous Cu found in the literature which claim to exhibit high compressive strains. | 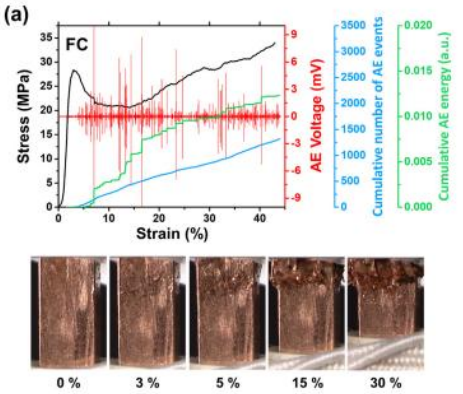 | [28] |
| Space holder | 16 | 70.2-77.1 | 1.2-2.3 | 50 | Conversely, ductile compression exhibits no drop in stress and maintains a smooth profile. Flow stress increases with increasing compressive strain. Photographs correlate with ductile compression of well over 30 % strain. | 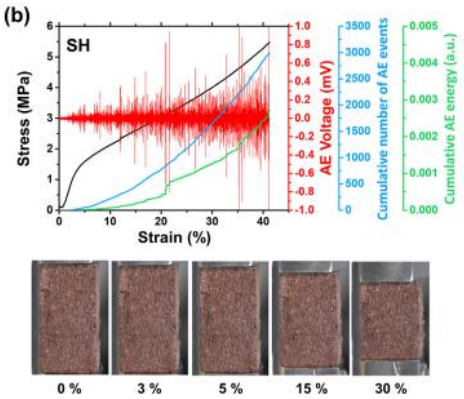 | [28] |

| Fabrication method | Strut diameter (µm) | Porosity (%) | Compressive strength (MPa) | Compressive strain (%) | Comments | Extracted figures | Ref |
|---|---|---|---|---|---|---|---|
| Space holder | >500 | 75-85 | ~25-35 MPa | 65-70 | Ductile, high strain to failure. | 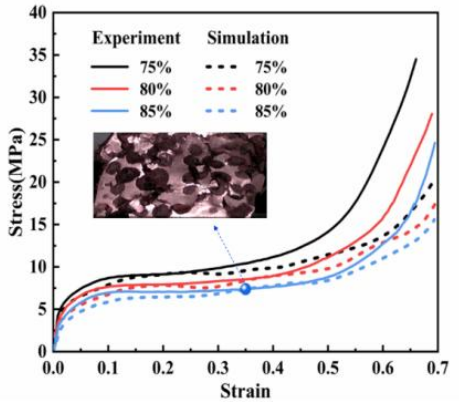 | [29] |
| Electro-deposition | ~500-1000 | 90.3-96.4 | ~2-11 | Approaching 50 % | Ductile, high strain to failure. Large porosities as high as 96.4 %. | 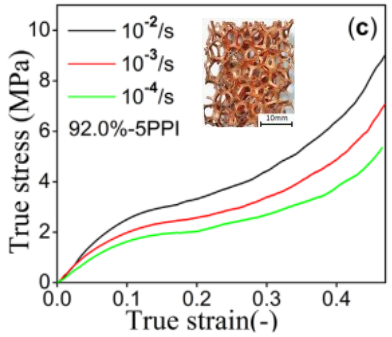 | [30] |

| Fabrication method | Strut diameter (µm) | Porosity (%) | Compressive strength (MPa) | Compressive strain (%) | Comments | Extracted figures | Ref |
|---|---|---|---|---|---|---|---|
| Selective laser metaling (SLM) | ~500-1000 | 80-90 | 1.84-12.83 | ~30(stress plateau) | Composition modified to improve printability using a laser power source (Cu-0.6Cr-0.4Zr, wt.%)<br><br>Ductile compressive stress-strain response.<br><br>Compressive strength defined as the first observation of a stress plateau in the stress-strain graph. | 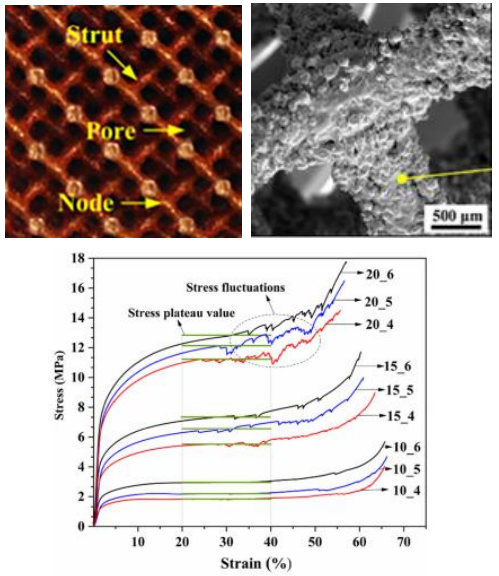 | [31] |
| Electroless deposition | ~505 | 88.2 | 0.8 | 8 | Low stress and strain at the stress plateau due to unoptimized electroless deposition of the relatively brittle Cu foam. | 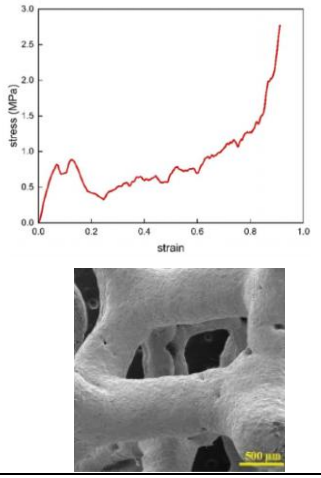 | [32] |

| Fabrication method | Strut diameter (µm) | Porosity (%) | Compressive strength (MPa) | Compressive strain (%) | Comments | Extracted figures | Ref |
|---|---|---|---|---|---|---|---|
| Laser powder bed fusion (PBF-LB/M) | 328 – Octet-truss (Oct)<br>347 – Cuboctahedron (Cub) | 62 – Oct<br>79 - Cub | ¬50 - Oct<br>¬15 - Cub | ¬50 | Ductile and strong Oct and Cub Cu structures. Compressive strength increased considerably with increasing strain rate. | 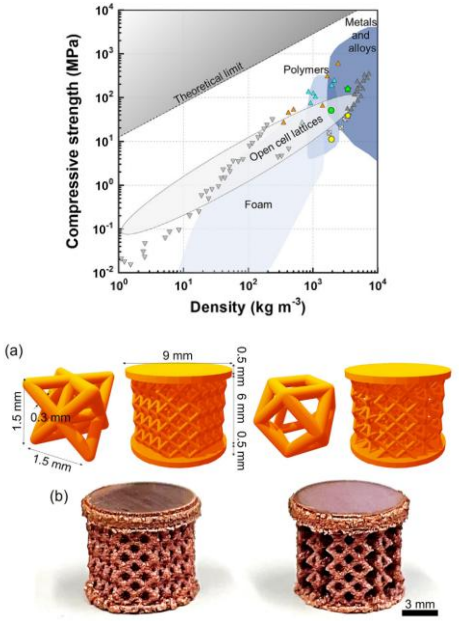 | [33] |
| PBF-LB/M | - | 70 | ¬50 – 1 % $LaB_6$<br>¬10 - Cu | ¬60 | Ductile and strong. Addition of 1 % $LaB_6$ resulted in a large increase in compressive strength while retaining high ductility. | 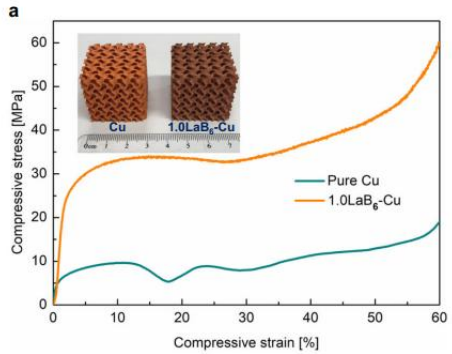 | [34] |

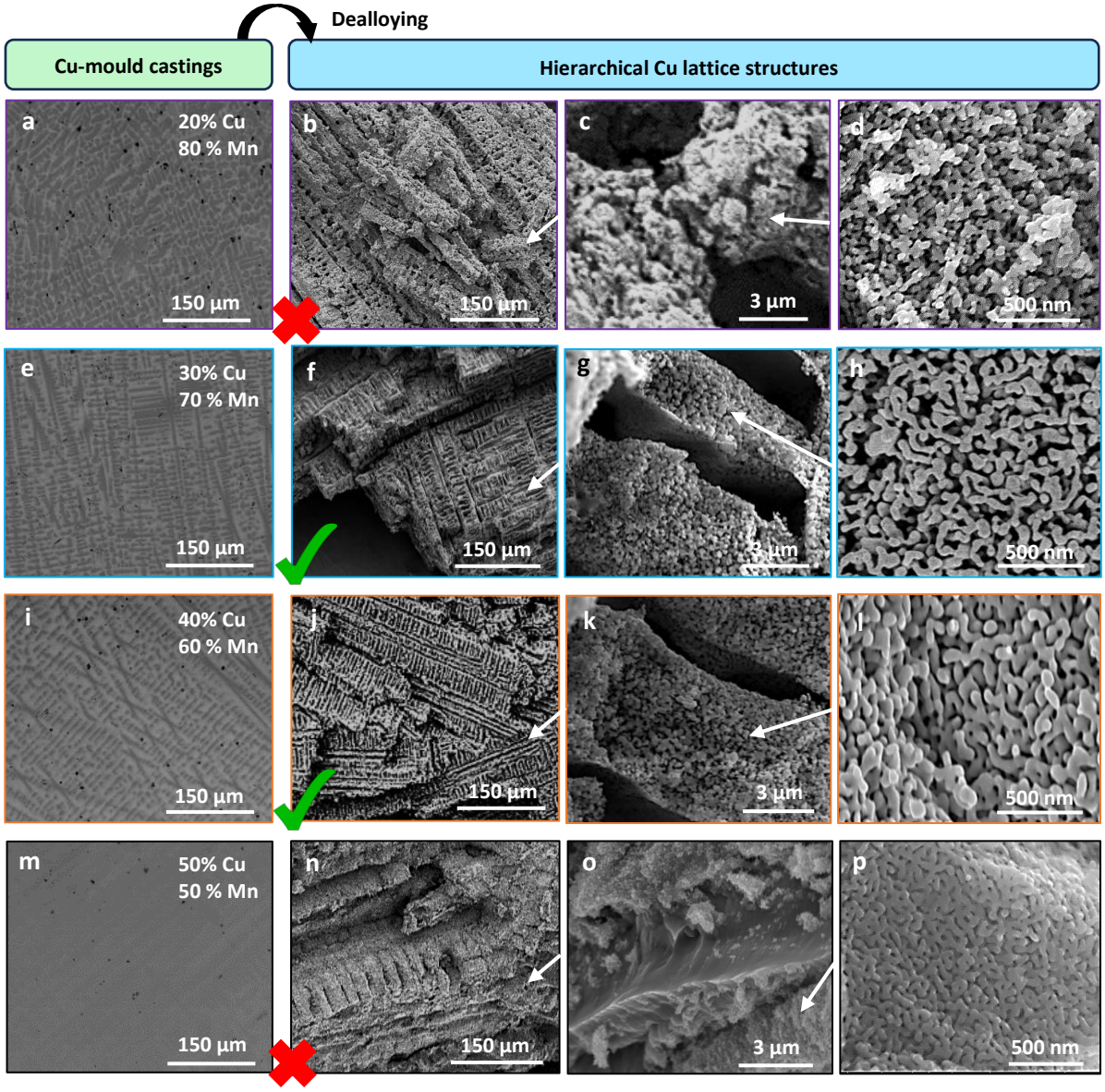


**Fig. S1:** Low-magnification BSE micrographs of the Cu mould-cast precursor alloy microstructures, alongside cross-sectional secondary electron (SE) micrographs of the as-dealloyed Cu structures obtained after dealloying in a 1 M HCl solution at 60°C. **a-d,** Mn-20Cu, **e-h,** Mn-30Cu, and **i-l,** Mn-40Cu reveal a hierarchical, lattice-like Cu structure with struts composed of nanoligaments. The Mn-20Cu specimens exhibited significant cracking and fragmentation during handling. **m-p,** Mn-50Cu specimens displayed a composite structure consisting of nanoligaments surrounding an undealloyed Cu-rich matrix. Green ticks mark suitable compositions, while red crosses indicate unsuitable ones.

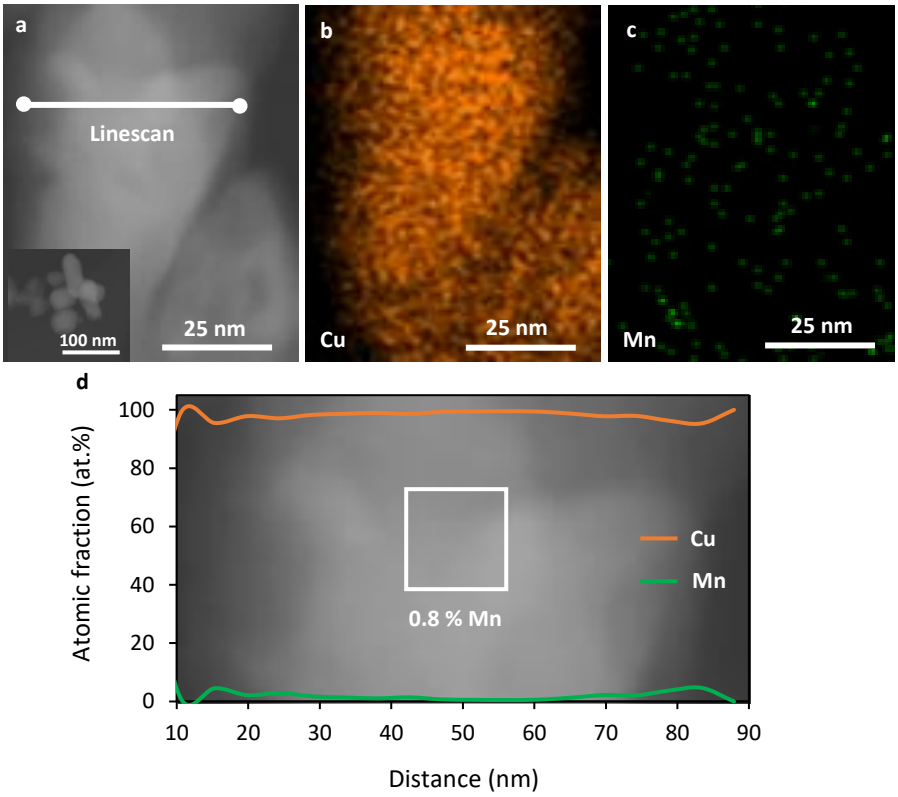


**Fig. S2: a,** Representative scanning transmission electron microscopy (STEM) micrograph of an isolated nanoligament obtained from the dealloying of a Mn-40Cu alloy in a 1 M HCl solution at 60 ˚C. Inset: Nanoligament cluster. **b,** Cu and **c,** Mn energy dispersive X-ray spectroscopy (EDS) maps. **d,** EDS linescan shows the atomic fractions of Cu and Mn elements across the thickness of the nanoligament. Selected area EDS analysis in the core of the nanoligament shows a residual Mn content of only 0.8 %, validating the success of the dealloying process.

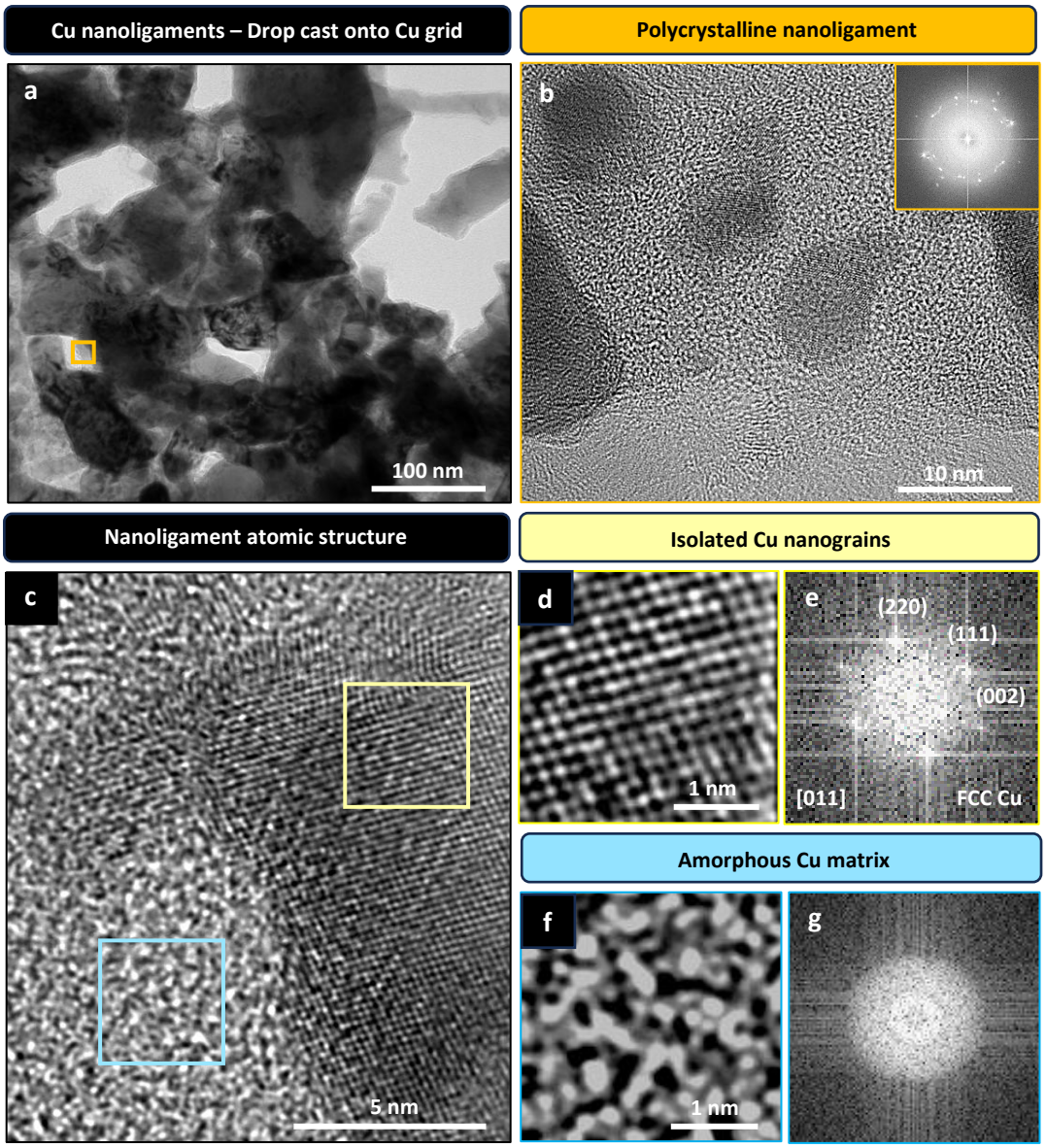


**Fig. S3: a,** Bright-field (BF) TEM micrograph of as-dealloyed Cu nanoligaments drop-cast onto a Cu grid. **b,** High-resolution TEM (HRTEM) micrograph of an isolated nanoligament reveals multiple nanograins (**inset:** fast Fourier transform (FFT) shows a dotted ring pattern indicative of disoriented grains). **c,** HRTEM micrograph of the nanoligament microstructure highlights misoriented nanograins embedded within an amorphous matrix. **d, e,** High-magnification HRTEM micrograph confirms the repeating lattice structure as face-centred cubic (FCC) Cu through indexed FFT analysis. **f, g,** High-magnification HRTEM micrograph of the amorphous Cu matrix is validated by the FFT, which displays a diffuse ring pattern.

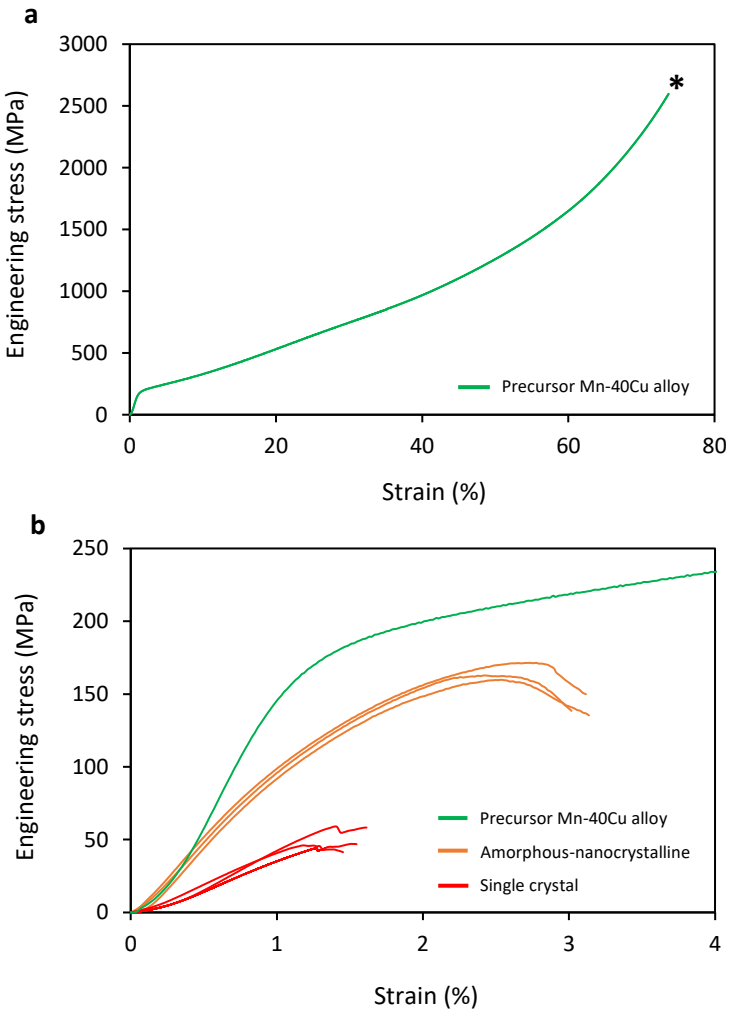


**Fig. S4: a,** Engineering stress-strain curves obtained from compression testing of the ductile Mn-40Cu precursor alloy. **b,** Comparative analysis of the Mn-40Cu precursor alloy, amorphous-nanocrystalline specimens dealloyed in a 1 M HCl solution at 60°C, and single-crystal specimens dealloyed in a 0.1 M HCl solution at 20°C. Compression tests were conducted on cylindrical samples (10 mm in height and 5 mm in diameter) at a displacement rate of 0.01 mm/s. Statistical reliability was ensured by testing a minimum of three specimens per condition. *Denotes exceeding of the 50 kN maximum force capacity of the compression testing machine

## *References*


1. Lührs, L. and J. Weissmüller, *Nanoporous Copper-Nickel – Macroscopic bodies of a strong and deformable nanoporous base metal by dealloying.* Scripta Materialia, 2018. **155**: p. 119-123.
2. Zhong, Y., et al., *Crack Mitigation during Dealloying of Au25Cu75.* Advanced Engineering Materials, 2014. **16**(4): p. 389-398.
3. Kong, Q., et al., *Fabrication and compression properties of bulk hierarchical nanoporous copper with fine ligament.* Materials Letters, 2014. **127**: p. 59-62.
4. Chen, F., et al., *Fabrication and mechanical behavior of bulk nanoporous Cu via chemical de-alloying of Cu–Al alloys.* Materials Science and Engineering: A, 2016. **660**: p. 241-250.
5. Ma, H., et al., *Influence of dealloying solution on the microstructure of nanoporous copper through chemical dealloying of Al75Cu25ribbons.* Journal of Materials Research, 2020. **35**(19): p. 2610-2619.
6. Hayes, J.R., et al., *Monolithic nanoporous copper by dealloying Mn–Cu.* J Mater Res, 2006. **21**(10): p. 2611-2616.
7. Lee, S.-Y., et al., *Fabrication of high-strength duplex nanoporous Cu by dealloying a dual-phase Mg–Cu precursor alloy.* Journal of Magnesium and Alloys, 2020. **8**(3): p. 910-916.
8. Shi, S., et al., *Scaling behavior of stiffness and strength of hierarchical network nanomaterials.* Science, 2021. **371**(6533): p. 1026-1033.
9. Mbarek, W., B., et al., *Dealloying of Cu-Mg-Ca Alloys.* Metals 2018. **8**(919).
10. Tan, F., et al., *Potentiostatic Dealloying Fabrication and Electrochemical Actuation Performance of Bulk Nanoporous Palladium.* Metals, 2022. **12**(12).
11. Chen-Wiegart, Y.-c.K., et al., *Effect of Ag–Au composition and acid concentration on dealloying front velocity and cracking during nanoporous gold formation.* Acta Mater, 2013. **61**(15): p. 5561-5570.
12. Qi, Z., et al., *Formation and Characterization of Monolithic Nanoporous Copper by Chemical Dealloying of Al-Cu Alloys.* J Phys Chem C, 2009. **113**(16): p. 6694-6698.
13. Zhao, C., et al., *Fabrication and characterization of monolithic nanoporous copper through chemical dealloying of Mg–Cu alloys.* Corros Sci, 2009. **51**(9): p. 2120-2125.
14. Aburada, T., J.M. Fitz-Gerald, and J.R. Scully, *Synthesis of nanoporous copper by dealloying of Al-Cu-Mg amorphous alloys in acidic solution: The effect of nickel.* Corrosion Science, 2011. **53**(5): p. 1627-1632.
15. Wang, L., et al., *High-strength hierarchical-structured bulk nanoporous Cu prepared by dealloying and spark plasma sintering.* Scripta Materialia, 2021. **203**.
16. Yue, X., et al., *Three-dimensional nanoporous copper with tunable structure prepared by dealloying titanium–copper–cobalt metallic glasses for supercapacitors.* Micro & Nano Letters, 2020. **15**(5): p. 283-286.
17. Zhang, R., et al., *Formation mechanism of nanoporous silver during dealloying with ultrasonic irradiation.* RSC Adv, 2019. **9**(18): p. 9937-9945.
18. Ibrahim, S., et al., *Nanoporous Copper Ribbons Prepared by Chemical Dealloying of a Melt-Spun ZnCu Alloy.* The Journal of Physical Chemistry C, 2021. **126**(1): p. 212-226.
19. Liu, W., et al., *Formation of Monolithic Nanoporous Copper with Ultrahigh Specific Surface Area through Chemical Dealloying of Mg-Cu Alloy.* Int J Electrochem Sci, 2012. **7**: p. 9707-9716.
20. Zhang, Y., et al., *In-situ X-ray diffraction study on dealloying: A scenario of a Cu90Au10 alloy.* Journal of Physics and Chemistry of Solids, 2021. **150**.
21. Ji, Y., et al., *The Mechanical Characteristics of Monolithic Nanoporous Copper and Its Composites.* Advanced Engineering Materials, 2018. **20**(10).
22. Hengge, E., et al., *Porosity evolution and oxide formation in bulk nanoporous copper dealloyed from a copper-manganese alloy studied by in situ resistometry.* Nanoscale Adv, 2023. **5**(2): p. 393-404.
23. Li, M., et al., *Controllable nanoporous copper synthesized by dealloying metallic glasses: New insights into the tuning pore structure and applications.* Chemical Engineering Journal, 2022. **427**.
24. Hemmendinger, K.D. and A.M. Hodge, *Progression of the dealloying front in bilayer Cu–Al and Cu–Zn nanoporous foams.* Journal of Materials Research, 2023. **38**(13): p. 3407-3415.

25. Yanfei, Y.A.O., et al., *Microstructures and mechanical properties of bulk nanoporous copper fabricated by dealloying Al-Cu alloys.* Jorunal of Functional Materials, 2016. **47**(5): p. 180-184.
26. Sun, S., et al., *Synthesis, characterization, and dealloying of Al-Cu alloys prepared using spark plasma sintering.* IOP Conference Series: Materials Science and Engineering, 2022. **1249**(1): p. 012033.
27. Li, J., et al., *Fabrication and characterization of bulk nanoporous copper by dealloying Al–Cu alloy slices.* Corrosion Science, 2015. **90**: p. 216-222.
28. Hong, K., et al., *Comparison of morphology and compressive deformation behavior of copper foams manufactured via freeze-casting and space-holder methods.* Journal of Materials Research and Technology, 2021. **15**: p. 6855-6865.
29. Li, C., et al., *Multifunctional Open-Cell Copper Foam with Sphere Pores by a Modified Sintering–Dissolution Process.* Metals, 2023. **13**(4).
30. Chen, J., et al., *Study on the Compression Properties and Deformation Failure Mechanism of Open-Cell Copper Foam* Advanced Engineering Materials, 2017. **19**(11).
31. Ma, Z., et al., *Lattice structures of Cu-Cr-Zr copper alloy by selective laser melting: Microstructures, mechanical properties and energy absorption.* Materials & Design, 2020. **187**.
32. Besharati, F. and M.H. Paydar, *Fabrication of Copper Open Cell Foam by Electrochemical Deposition Method and Investigation on the Effect of Current Intensity and Plating Solution on the Created Microstructure.* Iranian Journal of Materials Forming, 2023. **10**(1): p. 4-12.
33. Kang, S.-G., et al., *Green laser powder bed fusion based fabrication and rate-dependent mechanical properties of copper lattices.* Materials & Design, 2023. **231**: p. 112023.
34. Liu, Y., et al., *Manufacturing of high strength and high conductivity copper with laser powder bed fusion.* Nature Communications, 2024. **15**(1): p. 1283.